



Highly-sensitive single-step sensing of levodopa by swellable microneedle-mounted nanogap sensors

SeungHyun Park^{a,1}, Yong Jae Kim^{a,c,1}, Elisabeth Kostal^b, Volha Matylitskaya^b, Stefan Partel^{b,**}, WonHyoun Ryu^{a,*}

^a Department of Mechanical Engineering, Yonsei University, 50 Yonsei-ro, Seodaemun-gu, Seoul, 03722, Republic of Korea

^b Research Centre for Microtechnology, Vorarlberg University of Applied Sciences, 6850, Dornbirn, Austria

^c Department of Electrical and Computer Engineering, North Carolina State University, Raleigh, NC, 27695, USA

ARTICLE INFO

Keywords:

Microneedle
Nanogap sensor
Redox cycling
Levodopa
Parkinson's disease
Methacrylated hyaluronic acid

ABSTRACT

Microneedle (MN) sensing of biomarkers in interstitial fluid (ISF) can overcome the challenges of self-diagnosis of diseases by a patient, such as blood sampling, handling, and measurement analysis. However, the MN sensing technologies still suffer from poor measurement accuracy due to the small amount of target molecules present in ISF, and require multiple steps of ISF extraction, ISF isolation from MN, and measurement with additional equipment. Here, we present a swellable MN-mounted nanogap sensor that can be inserted into the skin tissue, absorb ISF rapidly, and measure biomarkers *in situ* by amplifying the measurement signals by redox cycling in nanogap electrodes. We demonstrate that the MN-nanogap sensor measures levodopa (LDA), medication for Parkinson disease, down to 100 nM in an aqueous solution, and 1 μ M in both the skin-mimicked gelatin phantom and porcine skin.

1. Introduction

Parkinson's disease (PD) is a progressive neurological disorder with a neuronal loss of the substantia nigra (Tolosa et al., 2006). PD patients suffer from movement disorders such as hypoactivity, poor balance, and poor motor coordination (Senel et al., 2020). Levodopa (LDA, L-3, 4-dihydroxyphenylalanine) is well known as pharmacological therapy for PD treatment. The optimal dosage of LDA to patients is important since excess LDA can lead to unfavorable fluctuations of the subject's motor and cognitive functions (Bézar et al., 2003; Svenningsson et al., 2015). The common strategy of LDA dosage determination is doctor's confirmation of patient's motor, but its accuracy is limited and diagnosis based on quantitative analysis is highly desired (Contin et al., 1997). For that reason, various detection methods such as high performance chromatography (Doležalová and Tkaczykova, 1999), chemiluminescence (He et al., 2007), electrophoresis (Zhao et al., 2007), and fluorescence (Wu et al., 2007) were employed to monitor the LDA concentration in the human body. These strategies also have limitations, such as the need for an extra sampling process and complex equipment,

the time expenditure, and cost issues.

To address these issues, recently, electrochemical sensors for LDA detection were widely introduced, including wearable sweat band sensors (Tai et al., 2019), nanospheres-integrated sensors (Guo et al., 2020), screen-printed electrode based sensors (Brunetti et al., 2014; Yu et al., 2020), and MWCNT modified sensors (Babaei and Babazadeh, 2011). Electrochemical analyses have many advantages due to their prompt response, simple equipment, higher sensitivity and selectivity as well as being cost-efficient, and while allowing facile miniaturization with lower required power. However, most electrochemical sensing platforms required additional processing steps which used the human serum from the extracted blood. To directly measure LDA levels *in situ* in the patient body, next generation electrochemical sensor systems that can extract and measure the biomolecules simultaneously were developed. Interstitial fluid (ISF) can be utilized to detect biomolecules since there is a high correlation of biomolecule concentrations between blood and ISF. Microneedles (MN) can easily access ISF under the skin barrier and either extract the ISF in a minimally invasive manner or detect the biomolecules *in situ* (Zhu et al., 2020b; Samant and Prausnitz, 2018).

* Corresponding author.

** Corresponding author.

E-mail addresses: stefan.partel@fhv.at (S. Partel), whryu@yonsei.ac.kr (W. Ryu).

¹ These authors equally contributed to the paper.

Such MN sensors demonstrated measurements of various biomolecules from ISF including glucose (Zhao et al., 2020; Zheng et al., 2020), lactate (Bollella et al., 2019b; Windmiller et al., 2011), nitric oxide (Keum et al., 2015), alcohol (Mohan et al., 2017), and dopamine (Park et al., 2022). MN detection of LDA has also been reported previously (Goud et al., 2019; Ren et al., 2021). However, clinically important LDA concentration in ISF can be lower than the sensitivity achievable by the previous works (Rocha et al., 2014).

Interdigitated electrode array (IDA) is introduced to measure biomolecules with high sensitivity by redox cycling. Neurotransmitters such as dopamine (DA), catechol, and LDA can be detected by redox cycling. In a previous work, 100 nM of DA measurement was achieved using IDA with a separate process of ISF extraction (Alayo et al., 2016). On the other hand, ISF extraction by MN has been proven as a highly efficient and minimally invasive method. In particular, swellable MN (sMN) showed rapid extraction of ISF with minimum damage to tissue. Swellable hydrogel such as methacrylated hyaluronic acid (MeHA) has been widely used for sMNs because of its biocompatibility and superior swelling behavior (Chang et al., 2017; GhavamiNejad et al., 2019).

In this study, we aimed to integrate the functions of ISF extraction and highly sensitive sensing by constructing an array of sMNs directly on top of an IDA sensor (Fig. 1). An sMN-mounted IDA (sMN-IDA) sensor system is composed of biomolecule extraction and measurement components. The sMN for rapid ISF extraction was fabricated using MeHA. The fast swelling and uptake behavior of MNs is suitable to detect the LDA and DA from subdermal ISF. After administration to the skin, hydrogel MNs rapidly extract ISF and swell. Biomolecules such as LDA or DA existing in the extracted ISF can diffuse through the swollen hydrogel network and finally reach to the IDA where the electrochemical detection of LDA or DA occurs. The extracted LDA or DA was measured on the surface of IDA via redox cycling. The sMN-IDA sensor showed a remarkably enhanced sensitivity for LDA and DA *in vitro* down to the concentration of 100 nM and 10 nM, respectively. Moreover, the sMN-IDA sensor also achieved a high sensitivity with a linear range of 1 μ M–10 mM in a gelatin phantom and *ex vivo* study with porcine skin. Our sMN-IDA sensor system overcomes the limitation of detection sensitivity for ISF sensing and demonstrated the possibility of *in situ* monitoring of biomolecules of low concentration in the skin ISF.

2. Materials and methods

2.1. Materials

Photoresist SPR 955CM 0.5 was purchased from micro resist technology GmbH, Berlin, Germany. The developer AZ726 MIF was purchased from Microchemicals GmbH, Ulm, Germany. The spin-coating was performed on a SUSS ACS200 from SUSS Microtec GmbH, Munich, Germany. The exposure was performed on a DWL66+ from Heidelberg Instruments GmbH, Heidelberg, Germany. For the dry etching step into silicon, using a gas chopping technique (SF_6 , C_4F_8), a deep reactive ion etching (DRIE) ICP system Adixon AMS100 from Alcatel Vacuum technology, France was used. The sputtering of the SiO_2 layer was carried out on a Oerlikon LLS EVO from Oerlikon Surface Solutions AG, Balzers, Liechtenstein. Gold, as an electrode material, was evaporated with a Univex 500 from Oerlikon Leybold Vacuum GmbH, Germany. SU8-3005 was used to define the measurement area and the contact pads. The SU8-3005 was purchased from micro resist technology GmbH, Berlin, Germany. The wafer was separated by a fs-laser dicing machine (3D-Micromac AG, Chemnitz, Germany). Polydimethylsiloxane (PDMS) elastomer and curing agent (Sylgard184 silicone elastomer kit, Dow Corning, MI, 126 USA) were purchased to fabricate MN negative molds. To synthesize the MeHA, Hyaluronic acid (HA) was purchased from Bloomage Freda Biopharm Co., Ltd. (cat. no. HA-TLM 20–40, Mw. 200 kDa–400 kDa). N,N-Dimethylformamide (DMF) (cat. no. 227056), methacrylic anhydride (MA) (cat. no. 276685), and photoinitiator (Irgacure 2959) were purchased from Sigma Aldrich. Sodium hydroxide (NaOH, cat. no. 7571–440, Daejung), sodium chloride (NaCl, Duksan), ethyl alcohol anhydrous, 99.9% (Daejung) were also purchased. For electrochemical analysis, DA (dopamine hydrochloride, cat. no. H8502), LDA (3,4-Dihydroxy-L-phenylalanine, cat. no. D9628), phosphate buffered saline (PBS, cat. no. P4417) were purchased from Sigma Aldrich and Ag/AgCl Ink for preparation of reference electrodes (cat. no. 011464) was purchased from BAS Inc.

2.2. Fabrication of interdigitated electrode array chip

The detailed fabrication process of the lift-off free nanogap IDA chip is described in a previous publication (Matylytskaya et al., 2018; Partel

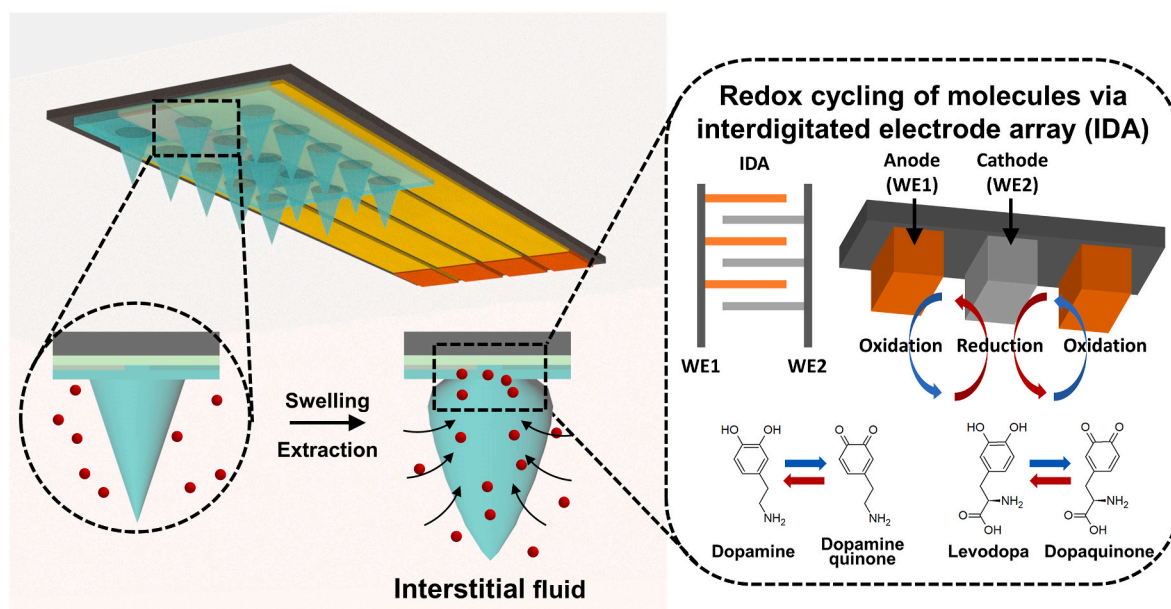


Fig. 1. Graphical abstract of sMN-IDA sensor that is composed of two components; biomolecule extraction components (left), electrochemical measurement components (right). Extraction of biomolecules in the ISF is conducted via MeHA MN swelling and the biomolecules are diffused and reached the surface of the electrode. The concentration of biomolecules was measured by the redox cycling of molecules via IDA.

et al. 2016, 2017). In general, the fabrication process consists of three main processes. The first process is to pattern the substrate. In this work, a laser direct writer was used to pattern the photoresist. A subsequent dry etching step transfers the pattern into silicon, which acts as an initial pattern. With the laser direct writer, feature sizes down to 600 nm were realized (write head 4 mm). These features were dry etched into silicon with a gas chopping process of SF_6 and C_4F_8 . After 52 s, we reached the desired etch depth of 1 μm . The remaining photoresist is removed by O_2 plasma. The second process step is to form an undercut and to create the nanogaps. The dielectric material SiO_2 was chosen for this step. A thickness of 700 nm SiO_2 results in a 500 nm gap at an initial structure of 1 μm . The smaller fabricated gap sizes show almost a linear behavior, which means that a 600 nm initial gap results in a 100 nm nanogap. The third step is to define the electrodes by a metal layer. This metal layer is evaporated on the substrate. In this work, a 100 nm thick gold layer was used as the final thickness of the electrode. Due to the undercut, which was created during the second step, the metal layers are electrically separated. In the next step, the measurement areas and the contact pads are defined by a dielectric layer. SU8-3005 is used and is spin-coated onto the substrate with a thickness of 5 μm . The exposure was carried out on a laser direct writer. The subsequent post exposure bake (2 min at 95 $^\circ\text{C}$) and the development (1 min in PGMEA in single puddle configuration) was done with the fully automated ACS200.

2.3. Methacrylation of hyaluronic acid

Synthesis of MeHA was carried out based on previously reported methods (Park et al., 2022). Briefly, 5.4 M of DMF and 91.3 mM of MA were sequentially added in the 2% of HA solution with stirring overnight. Subsequently, MeHA precursor gel was washed out 3 times using ethanol after dissolving 50 ml of 1 M NaOH while pH 8–9 was maintained. The dialysis process was performed with a dialysis tubing cellulose membrane (cat. no. D9777, Sigma Aldrich) containing the MeHA solution for a week. After dialysis, MeHA solution was lyophilized with a freeze dryer (FDU-2100, EYELA Singapore Pte. Ltd., Singapore) for 3 days and MeHA sponges were obtained for stable storage. The degree of methacrylation (DM) was measured by FT-NMR Spectrometer (AVANCE III HD 400, Bruker Biospin). The swelling ratio of the MeHA was calculated with the following equation, $\frac{W_s - W_d}{W_d} \times 100$, where W_s and W_d indicate the weight of hydrogel with swollen and dried state, respectively.

2.4. Electrochemical characterization and measurements

All electrochemical experiments were conducted using two potentiostat devices (CompactStat, Ivium software) (Fig. S1). Because the IDA chip has two working electrode (WE) pads, each WE pad was connected to each potentiostat while counter electrode (CE) and reference electrode (RE) pads were co-connected to CE and RE of both potentiostats, respectively. For cyclic voltammograms and simple chronoamperograms, only one potentiostat was operated, while the other one was disconnected. When two potentiostats were simultaneously operated to measure the redox cycling currents, an oxidation potential was applied to a WE and a reduction potential was applied to the other WE after 10 s from the oxidation started. In every measurement, the ground was maintained as floated to make the two potentiostats work independently without any electrical interruption.

2.5. Fabrication of sMN-IDA sensor

A mold for sMN was fabricated with a molding process. First of all, an aluminum MN array was prepared as a master mold by wire machining of $3 \times 3 \text{ cm}^2$ substrate. Each fabricated MN had a height of 600 μm , a base width of 400 μm , and a center-to-center distance of 600 μm . As a negative mold material, PDMS was utilized and prepared by mixing

elastomer and curing agent with 10:1 (w/w). The PDMS was poured on the master mold and cured for 24 h in ambient conditions. Then, the PDMS mold was partially masked with a Kapton tape to form the MN array only the electrode area of the IDA chip. The sMN-IDA sensor was fabricated using a transfer molding method based on previously reported methods (Lee et al., 2018; Park et al., 2018). The PDMS mold with exposure cavity of 4×6 MN array was then filled with 5% of MeHA solution (w/v). Then, MeHA was crosslinked by UV crosslinker (BLX-365, VILBER, France) with energy for 1.5 J/cm^2 and the surface of the IDA was treated by oxygen plasma to enhance hydrophilicity. An Ag/AgCl ink was applied on the RE area of the IDA chip and heated at 120 $^\circ\text{C}$ for 5 min. After aligning and contacting between the mold filled with the MeHA solution and electrode of the IDA chip, additional crosslinking of MeHA was performed with the energy of 1.5 J/cm^2 which is about the half energy for MeHA to fully crosslinked to form a hydrogel and attach with the IDA.

2.6. Preparation of in vitro phantoms and ex vivo porcine skin

A Gelatin phantom was fabricated by mixing a gelatin and the various concentrations of LDA in the PBS solution. The LDA from 1 μM to 10 mM were dissolved in the PBS firstly, and then the 1% (w/v) of gelatin powder (cat. no. G1890, Sigma Aldrich) was added with vigorous stirring for an hour at 60 $^\circ\text{C}$. The gelatin solution was poured into the Petri dish and stored in the refrigerator for the hardening of the gelatin phantom. For mimicking the epidermis, the one layer of parafilm was covered on the top surface of the gelatin phantom. Porcine skin was purchased from the local market. The porcine skin which contained various concentration of LDA was prepared based on previously reported methods (Park et al., 2022). Briefly, the fat layer of porcine skin was removed and cut into 2 cm \times 1 cm pieces. LDA from 1 μM to 10 mM in PBS solutions were prepared and the porcine skin was soaked into it. After 2 h, the porcine skin was taken out from the solution and the residual solution upon the surface was swiped away before measurement.

2.7. Imaging process

To characterize the gaps of each IDA and the geometry of the attached sMN array, a conventional scanning electron microscopy (SEM) (JSM-7001F and JSM-7610F, JEOL Ltd., Japan) was utilized. Unlike the IDA, since the attached sMN array was hydrogel, which is a dielectric material, the additional metal coating was applied using a metal coater (Sputter coater 108auto/SE, Cressington). The images of either a fabricated sMN or a penetrated sMN into the gelatin phantom were obtained with stereo microscopes. To measure the insertion depth of sMN, a histologic analysis was conducted. After *ex vivo* tests, the porcine skin was harvested and the cryo-block was prepared using an optimal cutting temperature (OCT) compound (Tissue-Tek, Sakura Finetek, USA). The cryosectioning with a thickness of 10 μm was performed and then the insertion wound was imaged by an inverted microscope.

2.8. Statistical analysis

The statistical analyses were performed with OriginPro (Originlab, USA) and Excel (Microsoft, USA). All data of the *in vitro* tests are presented as the mean \pm standard error of the mean. The statistical significance was evaluated with the Student's t-test; P-values of less than 0.05 were considered statistically significant.

3. Results

3.1. Fabrication and characterization of interdigitated electrode array

A nanogap IDA was fabricated by a lift off-free fabrication process which was introduced before (Partel et al., 2016). Briefly, an IDA pattern with a larger gap was fabricated using direct laser writing of spin coated

photoresist and subsequent deep silicon etching. After that, a narrowed nanogap between two electrodes was obtained by thermal oxide growth, then finally electrodeposited by a metalization step (Fig. 2A). The nanogap between each electrode was delicately controlled during the thermal oxide growth step. The fabricated IDAs were characterized using optical and electrochemical methods. The nanogaps of the microfabricated IDAs were measured using SEM images. The nanogaps were influenced by their processing conditions and intrinsic properties of the specimen, and they varied from 250 nm to 650 nm (Fig. 2B). The electrochemical activity and the redox cycling performance of the IDAs were also measured

using a model redox mediator, ferri/ferrocyanide ($\text{Fe}[\text{CN}]_6^{3-/4-}$). In the cyclic voltammetry (CV) measurement using $\text{Fe}[\text{CN}]_6^{3-/4-}$, each WE showed a clear oxidation/reduction behavior which indicated that each electrode of the IDA was electrochemically activated (Fig. 2C). Furthermore, redox cycling of $\text{Fe}[\text{CN}]_6^{3-/4-}$ at the IDA was demonstrated by applying the oxidation and reduction potential on each WE, separately. The redox current was measured as 50 μA during redox cycling while 0.1 μA was measured with only oxidation reaction, therefore the electrochemical current was amplified 500 folds by using redox cycling of the IDA (Fig. 2D and E).

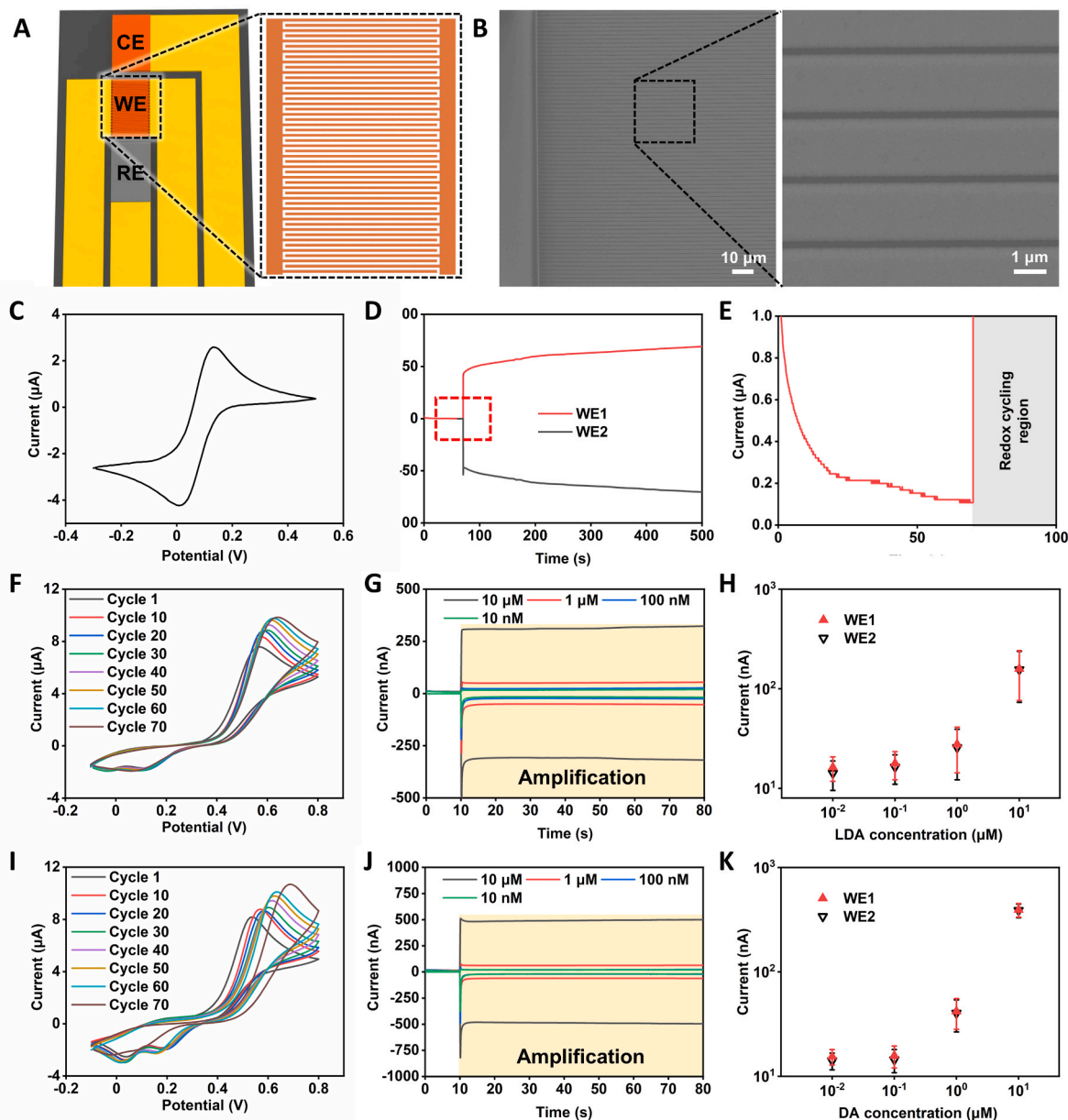


Fig. 2. Characterization of IDA chip. (A) Schematic images of the IDA chip with three electrodes; working (IDA, WE), counter (CE), and reference (RE) electrode. (B) SEM images of IDA and magnified nanogaps image. (C) Cyclic voltammogram of $\text{Fe}[\text{CN}]_6$ using IDA. (D) Chronoamperometric measurements using the IDA chip in $\text{Fe}[\text{CN}]_6$ by redox cycling. The WE1 (red curve) was set at an oxidation potential of 0.4 V vs. Ag/AgCl, while the WE2 (black curve) at a reduction potential of -0.1 V vs. Ag/AgCl. (E) The redox current was amplified 500 folds (gray region) using redox cycling of the IDA as shown by the magnified plots of the red box in (D). (F) Cyclic voltammograms of LDA (10 mM) with the increasing number of cycles. (G) Representative chronoamperograms using the IDA chip in LDA by redox cycling. Colored region represents the current amplification after applying the potential on the WE2. (H) Redox currents of each WE in 80 s of LDA with the concentration from 10 nM to 10 μM in 10-fold increments. All data are presented as mean \pm standard error ($n = 3$). (I) Cyclic voltammograms of DA (10 mM) with the increasing number of cycles. (J) Representative chronoamperograms using the IDA chip in DA by redox cycling. Colored region represents the current amplification after applying the potential on the WE2. (K) Redox currents of each WE in 80 s of DA with the concentration from 10 nM to 10 μM in 10-fold increments. All data are presented as mean \pm standard error ($n = 3$).

3.2. Synthesis of methacrylated hyaluronic acid

HA is a well-known biomaterial and used for many biomedical applications. However, since pristine HA easily dissolves in an aqueous solution, MeHA was synthesized to swell in aqueous conditions without dissolving. The hydroxyl group of the HA backbone was modified to methacrylate group. Briefly, 2% of HA solution was prepared, subsequently adding the DMF and MA for the methacrylate groups modification. The modification process was finished after ethanol washing and dialyzing. Synthesized MeHA solution was lyophilized before use. The DM was approximately 32% by calculating with the results of $^1\text{H-NMR}$ (Fig. S2A). MeHA with a photoinitiator was crosslinked by exposure to ultraviolet (UV) light before drying to fabricate an array of MNs. To measure the swelling behavior of synthesized MeHA, MeHA MN arrays were immersed in DI water, and the volume was measured at pre-determined time points. The swelling ratio of MeHA rapidly increased to 2,818% at 10 min and saturated at 3,169% after 30 min of swelling (Fig. S2B).

3.3. In vitro biomolecule detection using interdigitated electrode array

The performance of monitoring LDA and DA using the fabricated IDA without sMNs was conducted. Before measuring LDA using redox cycling amplification, the proper redox potential of each analyte should be determined. Therefore, a CV curve of LDA was measured with a potential range from -0.1 V to 0.8 V (Fig. 2F). Based on the redox peaks in the CV graph, 0.7 V and 0 V were selected as the oxidation and reduction potential of LDA, respectively. Using those potentials, amplified currents were measured by soaking the IDA in a PBS solution with different LDA concentrations from 10 μM down to 10 nM (Fig. 2G). The pH of the PBS solutions was set to 4.5 since the skin pH was known as acidic (Ali and Yosipovitch, 2013) and the LDA and DA were rapidly oxidized in the neutral pH condition. The redox cycling currents were amplified when both oxidation and reduction potential were applied on each WE and the amount of current varied with the LDA concentrations. The oxidation and the reduction currents had the similar current level but with opposite signs which indicated the anodic and cathodic current of LDA, respectively. 159 and 156 nA of redox cycling current was measured at both WEs, respectively, for a PBS solution with 10 μM of LDA. The current was proportional to the concentration of LDA, showing linearity as the concentration decreased to 16 and 14 nA at 10 nM (Fig. 2H). DA was also measured by following the procedure of LDA measurements. Since DA is a well-known neurotransmitter that is electrochemically reversible similar to LDA, it is suitable to use for the characterization of IDA redox cycling. Based on the CV plots as shown in Fig. 2I, 0.7 V and 0 V vs. Ag/AgCl were selected as the oxidation and reduction potential of DA, respectively. The redox cycling currents of various DA concentrations were measured by applying the selected potentials, 0.7 V (oxidation) and 0 V (reduction). At 10 μM of LDA solution, the redox cycling current of 483 and 413 nA was measured at both WEs, respectively, by cycling anodic and cathodic reactions (Fig. 2J). The current decreased to 25 and 23 nA as the DA concentration decreased to 10 nM. They also showed a linear relationship between the concentration and the measured currents as indicated in Fig. 2K. The chronoamperograms using the IDA in low concentrations of both LDA and DA showed significant current amplifications. When the LDA concentrations were 1 μM and 100 nM, and 10 nM, the current was amplified 239%, 134%, and 121% on the 1st WE (WE1) as well as 3,424%, 2,282%, and 2,038% on the 2nd WE (WE2), respectively. In case of DA detection, when the concentrations were 1 μM , 100 nM, and 10 nM, the current was amplified 335%, 98%, and 214% on WE1 as well as 12,512%, 8,411%, and 19,418% on WE2, respectively. The reason why there is a difference in the degree of amplification between WE1 and WE2 is that a higher non-faradaic current is generated before amplification because a higher potential (0.7 V) from the redox potential is applied to WE1.

3.4. Fabrication and characterization of swellable microneedle-mounted interdigitated electrode array sensors

To extract biomolecules in the skin ISF and deliver them to the electrode surface, sMN array were combined with IDA chips. The swelling of sMN leads to the rapid absorption of biomolecules such as LDA or DA in ISF into the sMNs. Then, they diffuse through the swelled MN and finally reach the surface of the IDA electrodes. Since the rapid volume expansion of sMNs can cause their detachment from the IDA surface, the IDA surface was modified by oxygen plasma to strengthen the adhesion between the sMN array and the IDA. Then, an MeHA MN array was transfer-molded on an IDA chip (Fig. 3A). Since the surface of the IDA chip was modified to have hydroxyl groups, the MeHA MN array was firmly anchored on the electrode with further treatment of UV crosslinking and drying. Each sMN-IDA sensor had a 4×6 MN array which covered the surface of IDA, CE and pseudo-RE (Fig. 3B). The robustness of the attached sMN array on the IDA was evaluated by a peeling test as depicted in Fig. 3C. For each peeling test-curve, two noticeable peaks were observed which indicated the first detachment and the complete detachment of the MeHA layer, respectively (Fig. 3D). In case of the non-treated samples, both peaks appeared at the earlier step of peeling displacement compared to the samples treated with oxygen plasma. The plasma treatment positively influenced the firm attachment of the MeHA layer on the IDA surface, and it was also statistically analyzed with the height of peak forces. As plotted in Fig. 3E, the peeling force of oxygen plasma-treated sMN-IDA sensors was 46.7 gf while the non-treated one had the peak force of 16.4 gf. The detailed quality of adhesion between the sMN and the IDA were also verified using SEM images (Fig. 3F). Without the surface treatment, the MeHA-sMN coating on the IDA was partially detached in multiple locations, while the surface-treated sample showed the firm and uniform adhesion of the MeHA-sMN layer on the IDA surface.

To confirm the functionality of the sMN-IDA sensor, an electrochemical characterization with $\text{Fe}[\text{CN}]_6^{3-/4-}$ was performed. 50 μL of an analyte solution was dispensed on an MeHA-sMN array. The CV analysis of a single electrode of the IDA showed clear oxidation and reduction peaks (Fig. 3G). It was noticeable that the CV peaks gradually increased for increasing number of cycles. This is due to the effect of gradual swelling of sMN after the analyte solution was dispensed on an sMN-IDA sensor. This leads to the increase of the analyte arriving at the IDA surface. Current amplification with redox cycling between two nanogap IDAs was also demonstrated by applying 0.4 V and -0.1 V to the two WEs of the IDA. Before granting the reduction potential, the anodic current was stabilized to approximately 0.2 μA . After both oxidation and reduction potential were activated, the current immediately jumped to approximately 100 μA , which was an amplification of 500 folds compared to single WE operation (Fig. 3H and I).

3.5. Levodopa and dopamine detection and selectivity

Before measuring LDA or DA using redox cycling amplification, the proper redox potential of each analyte should be determined. Therefore, CV analysis was performed for LDA (10 mM) (Fig. 4A). Based on the redox peaks in the CV graph, 0.7 V and 0 V were selected as the oxidation and reduction potential of LDA, respectively. With those potentials, amplified currents were measured by soaking the sMN array in PBS solutions with different LDA concentrations from 10 mM down to 100 nM (Fig. 4B). The redox cycling currents were amplified when both oxidation and reduction potential were applied on each WE at the same time and the amount of current varied with the LDA concentrations. The oxidation and the reduction currents had the similar current level but with opposite signs, which indicated anodic current and cathodic current, respectively. Approximately 28 μA of redox cycling current was measured with 10 mM of LDA on the sMN-IDA chip. The current is linearly proportional to the concentration of LDA ($R^2 = 0.99$) as the concentration decreased to about 0.003 μA at 100 nM (Fig. 4C). In

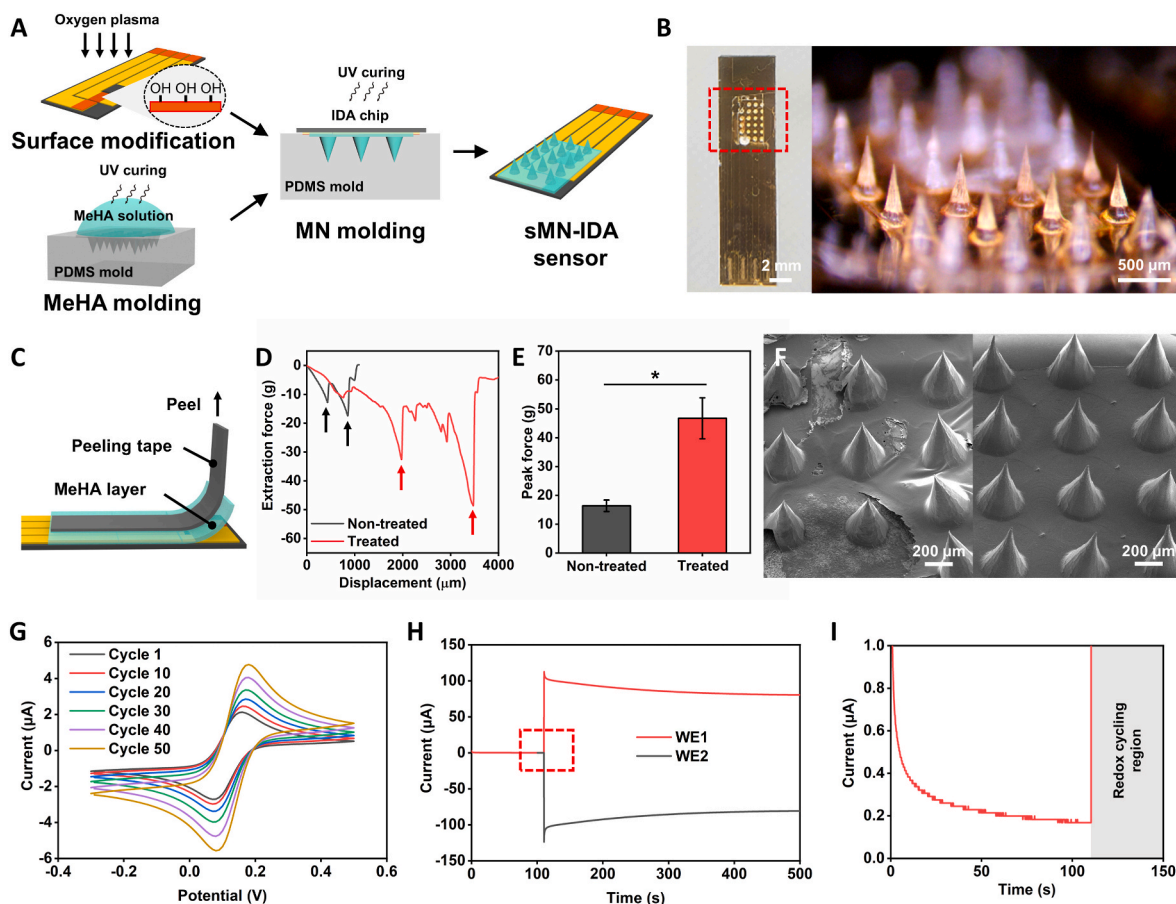


Fig. 3. Fabrication and characterization of the sMN-IDA sensor. (A) Schematic images of the sMN-IDA fabrication process. An IDA chip modified by hydroxyl groups and an sMN array was integrated by transfer molding. (B) Stereo microscopic images of the fabricated sMN-IDA sensor. (C) Schematic image of the peeling test. (D) Force vs. displacement curves and (E) peak force plots of the peeling test with non-treated and oxygen plasma-treated IDA chips. All data are presented as mean \pm standard error ($n = 4$). Statistical significances were analyzed using Student t-test, $*P < 0.05$. (F) SEM images of a non-treated and an oxygen plasma-treated sMN array on the IDA chip. (G) Cyclic voltammogram of a single electrode sMN-IDA sensor with $\text{Fe}[\text{CN}]_6$. (H) Chronoamperometric measurements using the sMN-IDA sensor in $\text{Fe}[\text{CN}]_6$ by redox cycling. (I) The redox current was amplified 500 folds (gray region) using redox cycling of the sMN-IDA sensor as shown by magnified plots of the red box in (H).

Fig. 4D, it showed that significant differences between 100 nM and 1 μM of LDA solution ($n = 4$). Raw data of repeated *in vitro* detection of low concentration of LDA (10 μM , 1 μM , and 100 nM) is represented in Fig. S3. To achieve the selective detection of LDA among other common biomolecules such as uric acid (UA) or ascorbic acid (AA), a spike test was conducted. As shown in Fig. 4E, even though 100 μM of UA or AA was applied on the 100 μM of LDA-soaked sMN array, just 6% and 8% of redox current increase was observed. DA was also measured by following the procedure of LDA measurements. Based on the CV plot as shown in Fig. S4A, 0.7 V and 0 V vs. Ag/AgCl were selected as the oxidation and reduction potential of DA, respectively. At 10 mM of DA solution, the redox cycling current of 59 μA was measured at both WEs by cycling anodic and cathodic reactions (Fig. S4B). The current decreased to 0.003 μA as the DA concentration decreased from 10 mM to 10 nM. The measurements also showed clear linearity ($R^2 = 0.99$) as indicated in Fig. S4C. As the results of selectivity test in Fig. S4D, 4.3% and 1.6% increments of redox cycling current were detected when 100 μM of UA or AA was added, respectively.

3.6. Analysis of levodopa in model phantom

Measurements of LDA in a model phantom were conducted to demonstrate the possibility of monitoring of the target species from human tissue. The skin-mimetic gelatin phantom which contained various concentrations of LDA molecules was prepared. The epidermis

and dermis of the skin tissue were mimicked by parafilm and 1% of gelatin block, respectively. The process of LDA detection is depicted in Fig. 5A. At first, sMN-IDA sensors are placed and aligned above the model phantom (Fig. 5B). The sMN-IDA sensor was inserted into the model phantom and electrochemical detection was conducted after 3 min swelling (Fig. 5C). The swelling behavior of the sMN was able to be observed through the transparent gelatin model phantom. After measuring, the sMN-IDA sensors were extracted from the phantom. The adhesion stability of the sMN-IDA sensors was confirmed, due to the fact, that all the sMNs swelled without being detached from the IDA chip (Fig. 5D). The amplified redox cycling current was measured with various LDA concentrations from 10 mM down to 1 μM (Fig. 5E, S6A,B). Saturated currents measured in 80 s were linearly proportional to the LDA concentration and showed high linearity ($R^2 = 0.97$ (WE1) and 0.99 (WE2)) (Fig. 5F).

3.7. Analysis of levodopa in porcine skin

The *ex vivo* measurement tests were performed using LDA-contained porcine skins. 2 h of immersion in an LDA solution allowed the porcine skin to absorb the LDA molecules in it. After sMN insertion, swelling for 3 min was required for LDA molecules to diffuse into the swollen sMN and to reach the surface of the IDA (Fig. 6A). Using the electrochemical measurement system in Fig. 6B, the sMN-IDA sensor was pressed to the LDA-contained porcine skin for 3 min (Fig. 6C). We were able to confirm

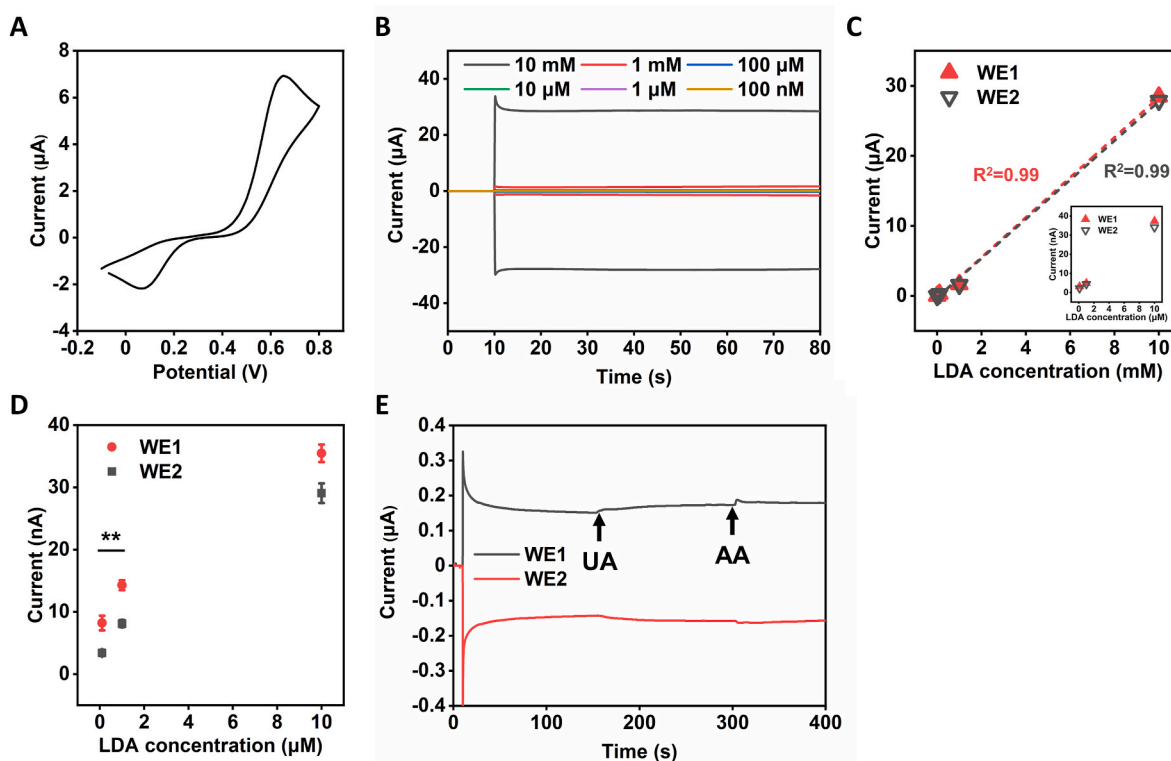


Fig. 4. *In vitro* detection of LDA with the sMN-IDA sensor. (A) Cyclic voltammogram of LDA (10 mM) using the sMN-IDA sensor. (B) Chronoamperometric measurements using the sMN-IDA sensor in LDA by redox cycling. (C) Redox currents of each WE in 80 s of LDA with the concentration from 100 nM to 10 mM in 10-fold increments. (D) Redox currents of each WE in 80 s of LDA with the low concentration of LDA (10 μM, 1 μM, and 100 nM). All data are presented as mean \pm standard error ($n = 3$ at 10 μM, $n = 4$ at 1 μM and 100 nM). Statistical significances were analyzed using Student t-test, $^{**}P < 0.01$. (E) Selective detection of LDA among other biomolecules (100 μM of UA and AA).

the insertion depth of the sMNs by histologic analysis. As shown in Fig. 6D, the sMN-IDA sensor successfully penetrated the epidermis and the insertion depth was 209 μm. The redox cycling current was also measured with various LDA concentrations from 10 mM down to 1 μM as the same process of *in vitro* phantom measurements (Fig. 6E, S6C,D). Saturated currents in 80 s after measurement was plotted in the current vs. LDA concentration plot and which showed a highly linear proportion to the LDA concentration ($R^2 = 0.99$) (Fig. 6F). The results showed that the immersion time of 2 h was sufficient to load the LDA in the skin tissue. In addition, the feasibility of a sMN-IDA was successively demonstrated by extracting and measuring LDA molecules from the skin *ex vivo*.

4. Discussion

As the second most common neurodegenerative brain disease in the world, with 6.3 million patients worldwide, PD degenerates behavioral functions and significantly damages the quality of life (Dinda et al., 2019). To diagnose and treat PD, there have been multiple attempts of developing biosensors. Recently, precise monitoring of an LDA level in the patient to determine the optimum dosage has been suggested as being critical (Brunetti et al., 2014; Goud et al., 2019). Although the precise detection of LDA can be achieved through traditional detection methods, electrochemical sensing is preferable for its rapid, precise, and simple process. Various sensor designs have been developed to measure the LDA electrochemically (Babaei and Babazadeh, 2011; Brunetti et al., 2014; Guo et al., 2020; Tai et al., 2019; Yu et al., 2020). Electrochemical methods such as square wave voltammetry, chronoamperometry, and differential pulse voltammetry measured electron transfer to the surface of a WE while a voltage bias was applied. To maximize the flow of the electron transfer from LDA to an electrode, electrode surface was

functionalized with various materials. Nanoparticles and CNT are effective ways to enhance the electron transport to the electrode surface by increasing the active surface area and conductivity of the WE (Baiao et al., 2018; Fouladgar et al., 2015). However, despite the surface functionalization, the minimum concentration of LDA detection was limited to 1 μM *in vitro* (Babaei and Babazadeh, 2011; Brunetti et al., 2014; Guo et al., 2020; Tai et al., 2019; Yu et al., 2020). However, when a 100 mg LDA tablet is administered to a patient, the plasma LDA concentration ranged from 451 nM to 5.31 μM (Rocha et al., 2014). This calls for more sensitive monitoring of LDA than the methods reported so far, considering even lower LDA concentration in ISF than in plasma. In addition, the presence of other ions and molecules such as UA and AA in ISF can cause the false detection of LDA, since the background molecules can be also easily electrochemically detected for a voltage bias applied for LDA.

To address these issues, we used the IDA to amplify electrochemical signals by redox cycling. The redox cycling is a method in which molecules amplify electron flow by applying different voltages to the WE1 and WE2 located close to each other as depicted in Fig. 1. Using the redox cycling reaction of LDA, this study achieved a detection sensitivity down to 100 nM *in vitro*, which is a lower concentration than the values reported previously (Table 1). The sMN can extract biomolecules rapidly and minimally invasively by the swelling behavior of hydrogels. Moreover, the proper geometry of sMN for skin penetration should be designed to swell and extract the molecules beneath the epidermis. Mechanically, since a center-to-center distance is related to the pressure applied to one MN, the wider the distance, the better the tissue penetration. Conversely, an appropriate distance is important because the number of MNs is proportional to the amount of ISF uptake. In our previous work, we used the same MN array which had a height of 600 μm, a base width of 400 μm, and a center-to-center distance of 600 μm

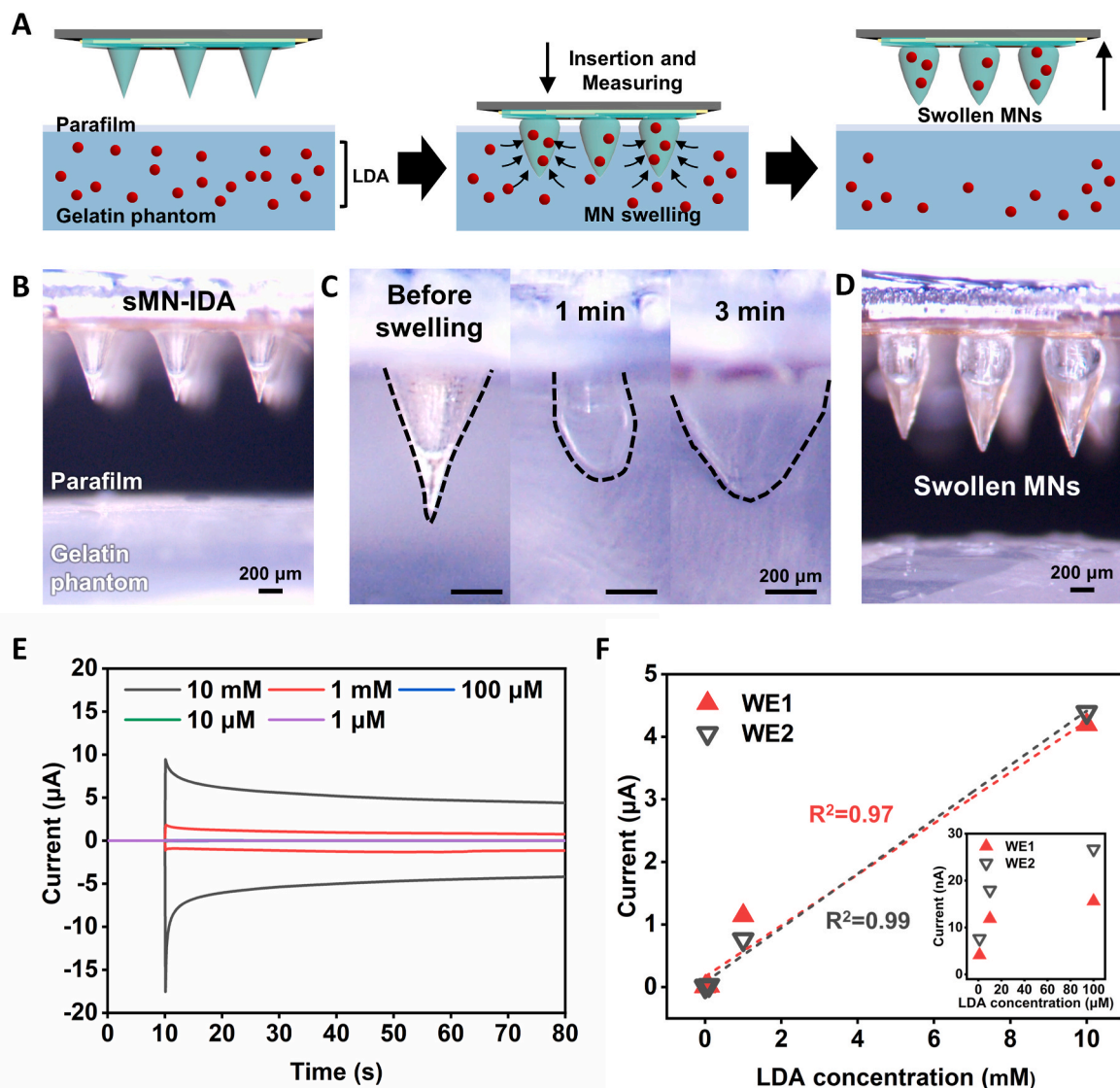


Fig. 5. Analysis of LDA in the model phantom. (A) Schematic images of the *in vitro* measurement test using the sMN-IDA sensor and the gelatin phantom which contained various concentrations of LDA. The sMN-IDA sensor was inserted into the gelatin phantom and measured after 3 min swelling. (B) Stereo microscopic images of the sMN-IDA sensor before insertion. (C) Swelling behavior of a sMN in the gelatin phantom in 3 min. (D) Stereo microscopic images of the swollen sMN-IDA sensor after the measurement. (E) Chronoamperometric measurements using the sMN-IDA sensor in gelatin phantom which contained LDA by redox cycling. (F) Redox currents of each WE in 80 s of LDA with the concentration from 1 μM to 10 mM in 10-fold increments. Inset plot represents the redox currents at 80 s of LDA with the concentration from 1 μM to 100 μM with 10-fold increments.

for ISF extraction (Park et al., 2022). This type of MN showed sufficient tissue penetration and excellent ISF extraction. In other papers, ISF extraction was also confirmed using MNs with similar dimensions (Zhu et al., 2020a; Chen et al., 2019; Xu et al., 2022). Although the skin penetration and ISF extraction of MeHA MN has been demonstrated in previous works (Alayo et al., 2016; Park et al., 2022), in this work, we attempted to combine MeHA MN and IDA to simultaneously extract biomolecules and measure their quantity. This integration system enables the 'single-step' measurement of LDA levels in our body without the need for additional post processes. This allows for PD patients, like diabetic patients, to control the frequency and amount of drugs through self-diagnosis after taking LDA. In addition, compared to continuous monitoring sensors, a short administration time minimizes side effects such as skin rash or biofouling of the electrode due to the long exposure to the ISF.

Fig. S5 shows a clear linearity in most of the concentration region. However, the linearity of the lowest concentration tends to decrease slightly when measuring LDA and DA. For low LDA or DA

concentrations, the ionic current response appeared more dominant than the redox cycling current from LDA or DA due to the decrease of the concentration, while ions in the solution had no change in concentration (MacFarlane et al., 2009). In order to estimate the ionic current, the following equation was employed.

$$I = z u v c F E A$$

The Einstein relationship can be used to estimate the migration-induced current, I , where z is the electron number of the ion, u is the ionic mobility, vc is the molar concentration, F is the Faraday constant, E is the electric field strength, and A is the electrode area. Here, PBS solution was used as a suspension, Cl^- is the most abundant ion in the solution. Therefore, 1 for z , 140 mM for vc , and $7.91 \times 10^{-8} \text{ m}^2/\text{sV}$ for u were selected accordingly. The area of electrode A was calculated as 0.28 mm^2 and E was calculated based on the potential difference of 0.7 V and the gap distance between each IDA. As a result, the ionic-migration-induced current between two WEs was estimated as 2.2 μA , which agrees with the first current value at the moment both potentials are

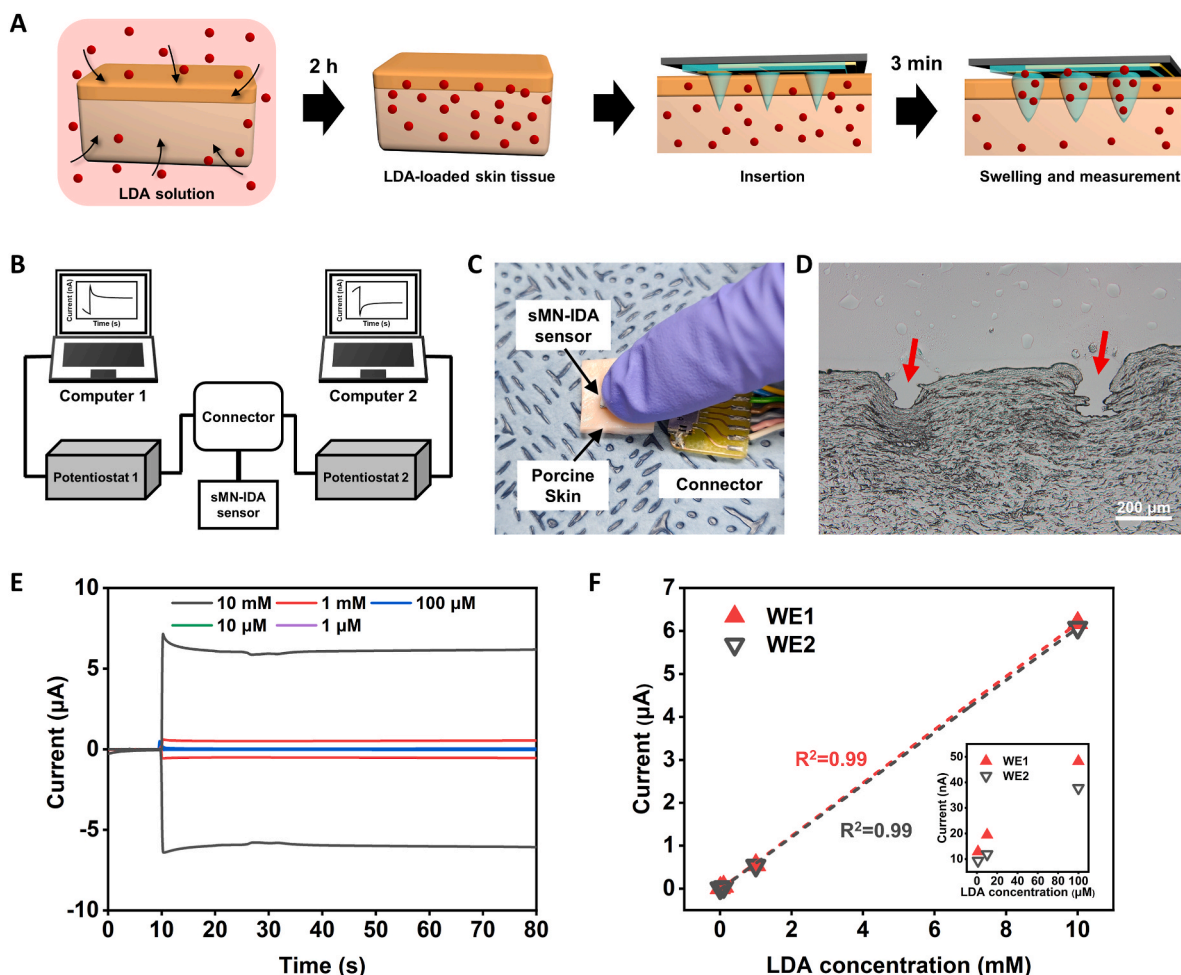


Fig. 6. *Ex vivo* analysis of LDA in porcine skin. (A) Schematic images of *ex vivo* measurement test using the sMN-IDA sensor and porcine skin which contained various concentrations of LDA. The sMN-IDA sensor was inserted into the porcine skin and measured after 3 min swelling. (B) Schematic images of the electrochemical experiment setup. (C) The sMN-IDA sensor being applied for 3 min to the porcine skin containing the LDA. (D) Histologic images of the porcine skin after applying the MeHA MNA. (E) Chronoamperometric measurements using the sMN-IDA chip in porcine skin which contained LDA by redox cycling. (F) Redox currents of each WE at 80 s of LDA with the concentration from 1 μM to 10 mM with 10-fold increments. Inset plot represents the redox currents at 80 s of LDA with the concentration from 1 μM to 100 μM with 10-fold increments.

applied on each WE. Therefore, the redox cycling current of LDA and DA was not distinguishable under 100 nM and 10 nM, respectively, since the ionic current had become dominant. The sensitivity could be improved by blocking the top surface of each electrode of the IDA, which reduces the effect of the ionic current and makes the redox cycling current along the edges of the IDA enhanced.

Since LDA and DA are natural biomolecules that are synthesized in the human body, as same as other biomolecules, LDA and DA could be oxidized and reformed multiple times (Fig. S7). Even though LDA has a reversible redox reaction dopaquinone, dopaquinone can close its extended branch to form a loop which is called cyclization. After this cyclization, dopaquinone changes to leucodopachrome, and it is an irreversible process. This leucodopachrome, a naturally oxidized specimen of LDA, has another reversible redox reaction with dopachrome (Byszewska and Kańska, 2014; Fatibello-Filho and da Cruz Vieira, 1997). As well as LDA, DA is also a reversibly reacting molecule with dopaminequinone, however, dopaminequinone moieties irreversibly transform to leucodopaminechrome by cyclization. Again, leucodopaminechrome has another reversible redox reaction with dopaminechrome (Bacil et al., 2020; Breczko et al., 2012). Because of these electrochemical properties of LDA and DA, continuously changing CV curves would be obtained which indicate the presence of irreversibly transforming reversible LDA or DA variants, thus, eventually, each CV

graph of LDA and DA has two oxidation and reduction peaks (Fig. 2F,I). Therefore, 0.7 V and 0 V vs. Ag/AgCl were selected to cover the entire redox reactions of LDA or DA, so that it was able to obtain the redox cycling signals of LDA, DA, and their variants successfully.

In the recent decade, a number of approaches have been investigated to fabricate MN-based transdermal electrochemical biosensors (Teymourian et al., 2021; Zhang et al., 2021). In order to combine MNs and electrochemical biosensors, most of the efforts were focused on functionalizing MNs with conductive materials (Gao et al., 2019; Rawson et al., 2019) or forming MNs with conductive materials (Mishra et al., 2020; Senel et al., 2019; Teymourian et al., 2019). However, these approaches demand post-functionalization of MN as an electrode or limited choice of MN materials. Furthermore, since metalization and electrical connection of individual MNs is challenging, multiple arrays of MNs had to be used as WE, CE, or RE. This results in wide distances among WE, CE, and RE, which normally lowers measurement sensitivity (Bollella et al., 2019a). On the other hand, in this study, a transfer molding technique was employed to combine IDA and sMN to utilize both advantages of IDA and sMN array in a single device. This direct attachment of the sMN array onto the IDA surface allows for fast uptake of biomolecules from ISF and subsequent highly-amplified measurement of target molecules, since the collected molecules by sMNs move fast to the surface of the IDA by both osmosis-driven convection and diffusion.

Table 1
Comparison of various electrochemical sensors for detection of LDA.

Electrodes	Methods	Detection range	Reference
Hollow microneedle array	Square wave voltammetry (non-enzymatic) Chronoamperometry (enzymatic)	<i>In vitro</i> (PBS): 5 – 300 μM (SWV) 20 – 300 μM (CA) <i>In vitro</i> (artificial-ISF): 20 – 360 μM (20 μM increments) (SWV) 20 – 300 μM (20 μM increments)(CA) <i>In vitro</i> (phantom): 50 – 200 μM (20 μM increments) (SWV & CA)	Goud et al. (2019)
Microneedle/spike-like Au Nanoparticles	Chronoamperometry	<i>In vitro</i> (PBS): 0 – 20 μM (2 μM increments) <i>In vitro</i> (serum): 0 – 10 μM (0, 2, 4, 6, 10 μM)	Ren et al. (2021)
PET substrate/Au layer/Au dendritic nanostructure	Cyclic voltammetry Chronoamperometry	<i>In vitro</i> (PBS): 0 – 1000 μM , 0 – 10 μM (0, 1, 2, 5, 10 μM)(CV) 0 – 5 μM (0, 1.25, 2.5, 5 μM) (CA) <i>In vitro</i> (sweat): 0 – 10 μM (0, 2.5, 5, 10 μM) (CV) 1.25 – 20 μM (1.25, 2.5, 5, 10, 20 μM)(CA)	Tai et al. (2019)
$\text{In}_2\text{S}_3\text{NSPs}/3\text{DGr}/\text{ITO}$ electrode	Differential pulse voltammetry	<i>In vitro</i> (PBS): 0 – 60 μM (0, 5, 10, 20, 40, 60 μM)	Guo et al. (2020)
Prussian blue carbon pasted screen-printed electrode	Cyclic voltammetry Chronoamperometry Coulometric response	<i>In vitro</i> (PBS): 0 – 10 μM (1, 3, 5, 10 μM)(CA) (Coulometric response) <i>In vitro</i> (serum): 1 – 10 μM (1, 3, 5, 10 μM) (Coulometric response)	Yu et al. (2020)
CNT-modified screen-printed electrode/poly (thionine) film/tyrosinase	Chronoamperometry	<i>In vitro</i> (PBS): 0.4 – 16 μM (0.4, 0.8, 2.3, 7, 16 μM) <i>In vitro</i> (serum): 0.8 – 22.3 μM (0.8, 2.3, 5.2, 14, 22.3 μM)	Brunetti et al. (2014)
Glassy carbon electrode/Multi-walled CNT/chitosan	Cyclic voltammetry Differential pulse voltammetry Chronoamperometry	<i>In vitro</i> (PBS): 2 – 220 μM (2, 4, 6, 10, 20, 30, 50, 80, 100, 140, 180, 220 μM)(DPV) 2 – 340 μM (2, 4 μM increments) (CA)	Babaei and Babazadeh (2011)

Table 1 (continued)

Electrodes	Methods	Detection range	Reference
Methacrylated hyaluronic acid microneedle/Au sputtered interdigitated electrode array	Chronoamperometry with redox cycling	<i>In vitro</i> (PBS): 0.1 – 10,000 μM (10 folds increments) <i>In vitro</i> (phantom): 1 – 10,000 μM (10 folds increments)	This work

Such direct building of sMN on a pre-built sensor unit can be utilized in many biosensor applications where sample collection can be done with MNs. sMNs can be attached directly on various types of sensors including electrochemical, optical, electrical, or mechanical sensors.

5. Conclusion

In this study, we developed an integrated swellable hydrogel-based MN and nanogap IDA sensors to measure redox cycling LDA in the skin ISF. The nanogap IDA sensors were constructed by three steps of lithographic processes. MeHA sMNs were built directly on a nanogap IDA sensor array by transfer molding. Electrochemical characterization and measurement using sMN-IDA sensors were performed using redox cycling molecules such as LDA and DA in solution and skin-mimicked gelatin phantom. Finally, we were able to measure LDA concentrations as low as 100 nM in an aqueous solution and 1 μM in both the gelatin phantom and porcine skin.

CRedit authorship contribution statement

SeungHyun Park: Conceptualization, Methodology, Validation, Investigation, Data curation, Writing – original draft, Writing – review & editing, Visualization. **Yong Jae Kim:** Methodology, Validation, Investigation, Data curation, Writing – original draft, Writing – review & editing, Visualization. **Elisabeth Kostal:** Investigation, Visualization. **Volha Matylitskaya:** Investigation, Visualization. **Stefan Partel:** Conceptualization, Resources, Writing – review & editing, Supervision, Project administration, Funding acquisition. **WonHyung Ryu:** Conceptualization, Resources, Writing – review & editing, Supervision, Project administration, Funding acquisition.

Declaration of competing interest

The authors declare that they have no known competing financial interests or personal relationships that could have appeared to influence the work reported in this paper.

Data availability

Data will be made available on request.

Acknowledgment

This work was supported by Global Infrastructure Program through the National Research Foundation of Korea (NRF) funded by the MSIT (2019K1A3A1A18116048), South Korea(W.R.), the National Research Foundation of Korea (NRF) grant funded by the Korea Government (MSIT) (2020R1A2C3013158), South Korea(W.R.), the Yonsei-KIST Convergence Research Program, South Korea(W.R.), and the Austrian Agency of Education and Internationalisation (OeAD) (KR 05/2020), Austria(S.P.).

Appendix A. Supplementary data

Supplementary data to this article can be found online at <https://doi.org/10.1016/j.bios.2022.114912>.

References

- Alayo, N., Fernández-Sánchez, C., Baldi, A., Esquivel, J.P., Borrisé, X., Pérez-Murano, F., 2016. *Microchim. Acta* 183 (5), 1633–1639.
- Ali, S.M., Yosipovitch, G., 2013. *Acta Derm. Venereol.* 93 (3), 261–269.
- Babaei, A., Babazadeh, M., 2011. *Electroanalysis* 23 (7), 1726–1735.
- Bacil, R.P., Chen, L., Serrano, S.H., Compton, R.G., 2020. *Phys. Chem. Chem. Phys.* 22 (2), 607–614.
- Baiao, V., Tomé, L.I., Brett, C.M., 2018. *Electroanalysis* 30 (7), 1342–1348.
- Bézar, E., Ferry, S., Mach, U., Stark, H., Leriche, L., Boraud, T., Gross, C., Sokoloff, P., 2003. *Nat. Med.* 9 (6), 762–767.
- Bolletta, P., Sharma, S., Cass, A.E.G., Antiochia, R., 2019a. *Biosens. Bioelectron.* 123, 152–159.
- Bolletta, P., Sharma, S., Cass, A.E.G., Antiochia, R., 2019b. *Electroanalysis* 31 (2), 374–382.
- Breczko, J., Plonska-Brzezinska, M.E., Echegoyen, L., 2012. *Electrochim. Acta* 72, 61–67.
- Brunetti, B., Valdés-Ramírez, G., Litvan, I., Wang, J., 2014. *Electrochem. Commun.* 48, 28–31.
- Byszeńska, W., Kańska, M., 2014. *J. Radioanal. Nucl. Chem.* 299 (3), 1373–1378.
- Chang, H., Zheng, M., Yu, X., Than, A., Seeni, R.Z., Kang, R., Tian, J., Khanh, D.P., Liu, L., Chen, P., 2017. *Adv. Mater.* 29 (37), 1702243.
- Chen, J., Wang, M., Ye, Y., Yang, Z., Ruan, Z., Jin, N., 2019. *Biomed. Microdevices* 21 (3), 1–10.
- Contini, M., Riva, R., Martinelli, P., Albani, F., Baruzzi, A., 1997. *Clin. Neuropharmacol.* 20 (5), 409–418.
- Dinda, B., Dinda, M., Kuls, G., Chakraborty, A., Dinda, S., 2019. *Eur. J. Med. Chem.* 169, 185–199.
- Doležalová, M., Tkaczyková, M., 1999. *J. Pharm. Biomed. Anal.* 19 (3–4), 555–567.
- Fatibello-Filho, O., da Cruz Vieira, I., 1997. *Analyst* 122 (4), 345–350.
- Fouladgar, M., Karimi-Maleh, H., Gupta, V.K., 2015. *J. Mol. Liq.* 208, 78–83.
- Gao, J., Huang, W., Chen, Z., Yi, C., Jiang, L., 2019. *Sensor. Actuator. B Chem.* 287, 102–110.
- GhavamiNejad, A., Li, J., Lu, B., Zhou, L., Lam, L., Giacca, A., Wu, X.Y., 2019. *Adv. Mater.* 31 (30), 1901051.
- Goud, K.Y., Moonla, C., Mishra, R.K., Yu, C., Narayan, R., Litvan, I., Wang, J., 2019. *ACS Sens.* 4 (8), 2196–2204.
- Guo, X., Yue, H., Huang, S., Gao, X., Chen, H., Wu, P., Zhang, T., Wang, Z., 2020. *J. Mater. Sci. Mater. Electron.* 31 (16), 13680–13687.
- He, W.W., Zhou, X.W., Lu, J.Q., 2007. *Chin. Chem. Lett.* 18 (1), 91–93.
- Keum, D.H., Jung, H.S., Wang, T., Shin, M.H., Kim, Y.E., Kim, K.H., Ahn, G.O., Hahn, S. K., 2015. *Adv. Healthc. Mater.* 4 (8), 1153–1158.
- Lee, K., Song, H.B., Cho, W., Kim, J.H., Kim, J.H., Ryu, W., 2018. *Acta Biomater.* 80, 48–57.
- MacFarlane, D.R., Forsyth, M., Izgorodina, E.I., Abbott, A.P., Annat, G., Fraser, K., 2009. *Phys. Chem. Chem. Phys.* 11 (25), 4962–4967.
- Matyilitskaya, V., Kasemann, S., Urban, G., Dincer, C., Partel, S., 2018. *J. Electrochem. Soc.* 165 (3), B127.
- Mishra, R.K., Goud, K.Y., Li, Z., Moonla, C., Mohamed, M.A., Tehrani, F., Teymourian, H., Wang, J., 2020. *J. Am. Chem. Soc.* 142 (13), 5991–5995.
- Mohan, A.V., Windmiller, J.R., Mishra, R.K., Wang, J., 2017. *Biosens. Bioelectron.* 91, 574–579.
- Park, S., Kim, Y.J., Park, S., Hong, H., Lee, J., Kim, S.I., Lee, K., Ryu, W., 2022. *Adv. Mater. Technol.* 7 (3), 2100874.
- Park, S.H., Jo, D.H., Cho, C.S., Lee, K., Kim, J.H., Ryu, S., Joo, C., Kim, J.H., Ryu, W., 2018. *Eur. J. Pharm. Biopharm.* 133, 31–41.
- Partel, S., Dincer, C., Kasemann, S., Kieninger, J., Edlinger, J., Urban, G., 2016. *ACS Nano* 10 (1), 1086–1092.
- Partel, S., Kasemann, S., Matyilitskaya, V., Thanner, C., Dincer, C., Urban, G., 2017. *Microelectron. Eng.* 173, 27–32.
- Rawson, T.M., Gowers, S.A., Freeman, D.M., Wilson, R.C., Sharma, S., Gilchrist, M., MacGowan, A., Lovering, A., Bayliss, M., Kyriakides, M., 2019. *The Lancet Digital Health* 1 (7), e335–e343.
- Ren, H., Mao, X., Zhang, S., Cai, Y., Xu, S., Fang, L., Ye, X., Liang, B., 2021. 2021 IEEE 16th International Conference on Nano/Micro Engineered and Molecular Systems (NEMS). IEEE, pp. 26–29.
- Rocha, J.-F., Falcão, A., Santos, A., Pinto, R., Lopes, N., Nunes, T., Wright, L.C., Vaz-da-Silva, M., Soares-da-Silva, P., 2014. *Eur. J. Clin. Pharmacol.* 70 (9), 1059–1071.
- Samant, P.P., Prausnitz, M.R., 2018. *Proc. Natl. Acad. Sci. USA* 115 (18), 4583–4588.
- Senel, M., Dervisevic, E., Alhassen, S., Dervisevic, M., Alachkar, A., Cadarso, V.J., Voelcker, N.H., 2020. *Anal. Chem.* 92 (18), 12347–12355.
- Senel, M., Dervisevic, M., Voelcker, N.H., 2019. *Mater. Lett.* 243, 50–53.
- Svenningsson, P., Rosenblad, C., af Edholm Arvidsson, K., Victorin, K., Keywood, C., Shankar, B., Lowe, D.A., Björklund, A., Widner, H., 2015. *Brain* 138 (4), 963–973.
- Tai, L.-C., Liaw, T.S., Lin, Y., Nyein, H.Y., Bariya, M., Ji, W., Hettick, M., Zhao, C., Zhao, J., Hou, L., 2019. *Nano Lett.* 19 (9), 6346–6351.
- Teymourian, H., Moonla, C., Tehrani, F., Vargas, E., Aghavali, R., Barfidokht, A., Tangkuaram, T., Mercier, P.P., Dassau, E., Wang, J., 2019. *Anal. Chem.* 92 (2), 2291–2300.
- Teymourian, H., Tehrani, F., Mahato, K., Wang, J., 2021. *Adv. Healthc. Mater.* 10 (17), 2002255.
- Tolosa, E., Wenning, G., Poewe, W., 2006. *Lancet Neurol.* 5 (1), 75–86.
- Windmiller, J.R., Zhou, N., Chuang, M.-C., Valdés-Ramírez, G., Santhosh, P., Miller, P.R., Narayan, R., Wang, J., 2011. *Analyst* 136 (9), 1846–1851.
- Wu, H.-P., Cheng, T.-L., Tseng, W.-L., 2007. *Langmuir* 23 (14), 7880–7885.
- Xu, N., Zhang, M., Xu, W., Ling, G., Yu, J., Zhang, P., 2022. *Analyst* 147 (7), 1478–1491.
- Yu, C., Cao, Q., Tu, T., Cai, Y., Fang, L., Ye, X., Liang, B., 2020. *J. Pharm. Biomed. Anal.* 190, 113498.
- Zhang, B.L., Zhang, X.P., Chen, B.Z., Fei, W.M., Cui, Y., Guo, X.D., 2021. *Microchem. J.* 162, 105830.
- Zhao, L., Wen, Z., Jiang, F., Zheng, Z., Lu, S., 2020. *RSC Adv.* 10 (11), 6163–6171.
- Zhao, S., Bai, W., Wang, B., He, M., 2007. *Talanta* 73 (1), 142–146.
- Zheng, M., Wang, Z., Chang, H., Wang, L., Chew, S.W., Lio, D.C.S., Cui, M., Liu, L., Tee, B. C., Xu, C., 2020. *Adv. Healthc. Mater.* 9 (10), 1901683.
- Zhu, J., Zhou, X., Kim, H.J., Qu, M., Jiang, X., Lee, K., Ren, L., Wu, Q., Wang, C., Zhu, X., Tebon, P., 2020a. *Small* 16 (16), 1905910.
- Zhu, J., Zhou, X., Libanori, A., Sun, W., 2020b. *Nanoscale Adv.* 2 (10), 4295–4304.